


Article

Tunable Ultraviolet Pulse Generation from a High-Power Self-Similar-Amplification Yb-Fiber Laser

Zefeng Wang , Daping Luo ^{*}, Gehui Xie, Zejiang Deng, Chenglin Gu and Wenxue Li ^{*}

State Key Laboratory of Precision Spectroscopy, East China Normal University, Shanghai 200062, China; 52200920017@stu.ecnu.edu.cn (Z.W.); ghxie@lps.ecnu.edu.cn (G.X.); zjdeng@lps.ecnu.edu.cn (Z.D.); clgu@lps.ecnu.edu.cn (C.G.)

^{*} Correspondence: dpluo@lps.ecnu.edu.cn (D.L.); wxli@phy.ecnu.edu.cn (W.L.)

Abstract: A tunable high-power 60 MHz ultraviolet pulse laser directly produced by the extra-cavity fourth-order harmonic generation of a self-similar amplification infrared pulse laser is reported in this study. Utilizing the self-similar pulse evolution and the self-phase modulation in a self-similar amplifier, the system generates a 58.9 W pulse train with a spectral half-width of 85.4 nm, corresponding to a pulse duration of 36 fs. To obtain the ultraviolet pulses from the infrared pulses, a single-pass frequency quadrupling system comprising two cascaded β -BBOs was used. The ultraviolet spectra can be tuned within a spectral range of 253.6 to 275 nm owing to the broadband infrared seed spectra. The maximum ultraviolet average power of 1.44 W was achieved at 275 nm with spectral half-width and an infrared-to-ultraviolet efficiency of 1.1 nm and 2.44%, respectively. To the best of our knowledge, this is the first demonstration of tunable high-power ultraviolet pulse generation from a self-similar amplification Yb-fiber laser.

Keywords: fourth-order harmonic generation; self-similar fiber amplification; ultraviolet pulse



Received: 14 December 2024

Revised: 3 January 2025

Accepted: 7 January 2025

Published: 8 January 2025

Citation: Wang, Z.; Luo, D.; Xie, G.; Deng, Z.; Gu, C.; Li, W. Tunable Ultraviolet Pulse Generation from a High-Power Self-Similar-Amplification Yb-Fiber Laser. *Photonics* **2025**, *12*, 50. <https://doi.org/10.3390/photronics12010050>

Copyright: © 2025 by the authors. Licensee MDPI, Basel, Switzerland. This article is an open access article distributed under the terms and conditions of the Creative Commons Attribution (CC BY) license (<https://creativecommons.org/licenses/by/4.0/>).

1. Introduction

Ultraviolet light (UV) refers to light with wavelengths ranging from 10 nm to 380 nm in a vacuum [1]. Tunable high-power pulses in the UV spectral range are used in a variety of applications, such as biochemical imaging [2,3], precision spectroscopy [4–7], atom trapping and cooling [8–11], and nanofabrication [12,13] because of their high photon energy, ultrashort duration, and small focus waist. Ultrahigh-power UV pulses can be directly generated using an excimer laser with a pulse duration of more than one picosecond [14,15]. In particular, a well-designed combination of a Ti:sapphire source and a KrF-gas-based amplifier can achieve both femtosecond duration and high power in the ultraviolet region at the cost of a large structure, low repetition rate, and limited operational time [16]. Furthermore, both the Ti:sapphire laser-based optical parametric amplifier [17] and the fiber-laser-pumped optical parametric oscillator [18,19] can produce tunable femtosecond pulses in a wide UV range. Moreover, the straight extra-cavity frequency conversion of a high-power fiber pulse laser allows for another method of accessing broadband UV spectra [20–23]. For example, UV pulses are generated using nonlinear media through third-order [24] and fifth-order [25] harmonic generation as well as chirped-pulse four-wave mixing [26], respectively. In general, nonlinear frequency conversion using gas or crystal media is an effective method for shifting visible and infrared pulses into the UV region [27–30]. Moreover, compared to using gas for generating UV pulses, employing

nonlinear crystals offers the advantages of a larger nonlinear coefficient and a simplified device structure [31].

The large surface-to-volume ratio and the broad emission bandwidth of the Ytterbium-fiber (Yb-fiber) ensure excellent heat dissipation and femtosecond-pulse generation, respectively. A Yb-fiber pulse laser with several cascaded fiber amplifiers is a practical alternative to the solid-state Ti:sapphire system because of its high pump efficiency, good beam quality, and high repetition rate, and it is widely used to generate high-power ultrashort infrared pulses, which provide an outstanding source laser for the generation of UV pulses. For example, through the cavity-enhanced quadrupling of high-power femtosecond pulses from a chirp-pulsed amplification (CPA) Yb-fiber laser, 1 W, 259 nm UV pulses have been demonstrated [32]. The spectral width of the amplified infrared pulses is limited to approximately ten nanometers because of the gain narrowing during the CPA, resulting in a finite spectral width of approximately 1 nm for the expectant UV pulses [33]. In contrast to CPA, self-similar amplification (SSA) can overcome the gain bandwidth limitation, resulting in shorter pulse duration and a wider spectrum. Mathematically, the nonlinear Schrödinger equation (NLSE) can be used to describe the pulse propagation in a fiber amplifier. Furthermore, the linear-chirped parabolic pulse is a mathematical asymptotic self-similar solution of the NLSE, indicating that the pulse can propagate by a constant parabolic intensity profile with the introduction of the linear chirp and power scaling in the fiber amplification [34,35]. Because of the nonlinear self-phase modulation (SPM) in the gain fiber, the output spectrum is broadened beyond the gain bandwidth. By further compensating for the linear chirp, high-power ultrashort pulses with broadband spectra can be achieved. In our previous study, high-power ultrashort infrared pulses with a spectral width of approximately 100 nm were achieved using a pre-chirping-management SSA system [36,37]. Thus, the SSA system offers a broadband ultrashort infrared source for tunable UV pulse generation.

In this study, a valid approach for generating tunable high-power UV pulses is demonstrated. This technique is achieved through extra-cavity fourth-order harmonic generation (FHG) of SSA-based infrared pulses. The system generates a 60 MHz infrared pulse train with average power, half spectral width, and duration of 58.9 W, 85.4 nm, and 36 fs, respectively, utilizing the self-similar evolution and SPM in the SSA. Frequency quadrupling to the UV region is achieved using two cascaded beta barium borate (β -BBO) crystals in the form of a single-pass configuration. It is highly possible to achieve the FHG because of the ultrashort infrared pulses and the high nonlinear coefficient of the β -BBOs. Owing to the ultra-wide spectra of the infrared pulses, the generated visible spectra can be tuned from 505 to 550 nm and the generated UV spectra can be tuned from 253.6 to 275 nm by fine-tuning the phase-matching angles of the β -BBO crystals. It was observed that the output power varies with the output UV wavelength, and the maximum ultraviolet output power of 1.44 W was achieved at 275 nm with a half spectral width of 1.1 nm and an infrared-to-ultraviolet efficiency of 2.44%.

2. Experimental Setups

The configuration of the SSA and FHG is shown in Figure 1, consisting of a seed laser, a fiber stretcher, two cascaded fiber pre-amplifiers, an SSA amplifier and a branch for wavelength conversion. A homemade 60 MHz nonlinear polarization rotation (NPR) mode-locked Yb-fiber oscillator with an output power of 20 mW was employed as the seed laser. The oscillator was able to operate in a stretched-pulse mode-locking regime and emit an infrared pulse train with a spectral width of 45 nm [38], by managing the cavity sum-dispersion at a net normal dispersion of 0.001 ps [39,40]. In order to isolate environmental disturbances, the entire cavity was encased in a multi-layered structure

comprising thermal insulation material, acoustic insulation cotton, and two high-density aluminum plates. Then, the infrared pulses were sufficiently stretched after transmitting in a 25 m single-mode fiber (SMF, HI 1060), to keep the next pre-amplifiers running under the linear amplification. Thus, pre-amplifiers can scale the power and energy without generating nonlinear chirps. In the first pre-amplifier, the infrared laser was amplified to 350 mW in a 0.8 m Yb-doped SMF, which was pumped by a 976 nm fiber-pigtailed semiconductor laser. Then, the second pre-amplifier was constructed with a 1.3 m polarization-maintaining large-mode-area Yb-doped photonic crystal fiber (PM LMA Yb-PCF), which was composed of 40 μm core and 200 μm inner cladding and was pumped by a 976 nm semiconductor laser in a backward pumping configuration. The large-mode-area photonic crystal fiber can significantly reduce nonlinear amplification distortion when it is used as a gain medium [41,42]. Two optical isolators (ISO) were inserted to avoid damage from the backward reflective light and the unabsorbed pumping light. After the two pre-amplifiers, the infrared pulses were scaled up to 8.4 W with a half spectral width of 14.7 nm. The spectra were clearly narrowed because of gain narrowing, which was caused by the finite gain bandwidth of the PM LMA Yb-PCF.

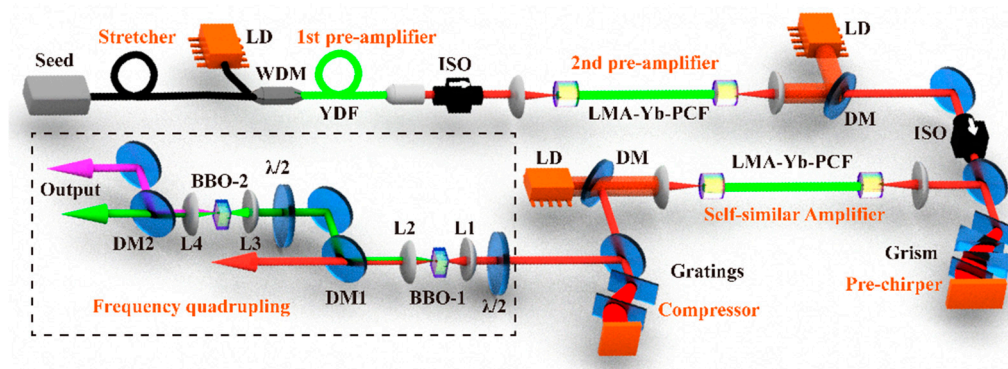


Figure 1. Experimental setup. ISO: isolator; LD: laser diode; YDF: Yb-doped fiber; WDM: wavelength-division multiplexing; DM: dichroic mirror; $\lambda/2$: half-wave plate; LMA Yb-PCF: large-mode-area Yb-doped photonic crystal fiber; L1, L2, L3, and L4: lens.

In contrast to a previous study [32], the second- and third-order dispersions generated in the fiber stretcher and CPA were compensated by a grism-based pre-chirper that consisted of a pair of transmission gratings (1000 L/mm groove density) and a pair of equilateral prisms (SF10) [33]. By finely adjusting the separation of the gratings and the insertion of the prisms, the secondary and tertiary dispersion produced in the grism could be changed to compensate for the chirps generated in the fiber stretcher and the CPA. Moreover, the grating and prism were placed with an incidence angle of 29.8° (Littrow angle) and 59.8° (Brewster angle), respectively. After the grism, the amplified pulses were compressed to approximately 150 fs with an output power of 4.2 W and compression efficiency of 50%. As shown in Figure 1, the SSA had the same structure as the second pre-amplifier despite a different fiber length of 1.6 m. Moreover, the PM LMA Yb-PCF in the SSA was mounted on a copper plate that was maintained at 20°C by a homothermal water-cooling setup. When the managed infrared pulses were delivered into the SSA to scale up the power, the spectra of the pulses were broadened because of the SPM in the amplification. Moreover, another pair of transmission gratings (620 L/mm groove density) was chosen to compensate for the linear chirps produced in the SSA. The appropriate separation of the gratings was adjusted to compensate for the different chirps generated at different powers in the SSA with a constant compression efficiency of 50%. In addition, to minimize back reflection, all the end faces of the PM LMA Yb-PCFs were polished at a slant angle of 8° . To avoid damage from

the backward reflective light and the unabsorbed pumping light, three optical isolators were inserted between the seed laser and the amplifiers.

In the frequency quadrupling system, two β -BBO crystals (type-I phase-matched) were used to perform nonlinear frequency conversion. The BBO-1 and BBO-2 were cut at 23.3° and 49.4° with a bulk size of $4 \times 4 \times 2 \text{ mm}^3$, supporting the second harmonic generations (SHGs) at near-infrared and green regions, respectively. Moreover, two cascade SHGs quadrupled the frequency, achieving FHG from infrared to UV. Specifically, the input infrared beam was focused on the first β -BBO crystal through L1. The generated second harmonic (SH) beam was then collimated by L2. Similarly, L3 and L4 were used to focus the SH beam on the second β -BBO crystal and collimate the generated UV beam. All the lenses (50 mm focal length) were mounted on a one-dimensional mobile platform to focus the infrared and the SH lights exactly at the centers of the first and second crystals, respectively. Furthermore, the crystals were configured on two 360° rotated mounts that could be tuned for phase-angle matching. Four dichroic mirrors were used to filter the unconverted infrared light and SH. Owing to the broadband nature of the fundamental wave, tunable UV output spectra were obtained by adjusting the phase-matching angles of the crystals.

3. Results and Discussion

Through the management of the second and third dispersions in the pre-chirper, the input pulses evolved following a self-similar scheme, resulting in linear chirp generation, power scaling, and spectral broadening. When the SSA pump power was increased to 200 W, infrared pulses with an average power of 117 W were obtained. After dispersion compensation in the grating compressor, the infrared pulses were effectively compressed at 50% efficiency, resulting in an output power of 58.9 W. To characterize the properties of infrared pulses, an optical spectrum analyzer (AQ6370, Yokogawa) and a commercial autocorrelator (Pulse Check, APE) were used to measure the spectra and pulse durations, respectively. As shown in Figure 2a, the autocorrelation trace of the compressed pulses is fitted by a sech²-type curve with a duration of 36 fs, which occurred at single-pulse energy of 1 μJ and peak power of 27.3 MW. The wings and bases were not observed in addition to the main pulse containing more than 98% pulse energy because the pulses were well managed by the grism and grating compressor. Figure 2b shows the output spectrum of the SSA at the same power, covering the spectral range from 1000 to 1120 nm with a half-width of 85.4 nm. After the cascaded fiber amplifiers, the spectral range is significantly broader than the seed oscillator, which facilitates the subsequent frequency quadrupling experiment to obtain a wider UV tuning range.

For the SHG of the infrared pulses, a 2 mm thick type-I interaction β -BBO crystal (BBO-1) that had a wide acceptance angle and could provide tunable SH spectra for UV generation was used. In order to improve the conversion efficiency of SHG [43,44], the distance between L1 and BBO-1 was accurately controlled to ensure that the infrared light was focused inside the center of BBO-1 with a calculated beam diameter of 30 μm . Then, a broadband infrared half-wave plate was added to the infrared beam to change the polarization state of the input pulses for high-quality SHG. Moreover, L2 was used to collimate the SH, and DM1 and DM2 were used to filter the unconverted infrared light. A 360° -rotated mount was used to adjust the crystal phase-matching angle. When this angle was set at 60° , a 550 nm SH was obtained. In this case, the output power and efficiency as functions of the incident infrared power are shown in Figure 3a. At an input power of less than 30 W, both the power and efficiency increased with the input power. By increasing the incident power to above 30 W, the output SH power increased with a slight increase in conversion efficiency; the maximum SH power of 8.98 W with a conversion efficiency

of 15.3% was obtained at an infrared power of 58.9 W. Generally, a broad spectrum of infrared laser cannot be entirely converted into visible. Therefore, the conversion efficiency was relatively low because the infrared spectrum width of 85.4 nm was much wider than the maximum output spectral width of the crystal. As shown in Figure 3b,c, through rotating BBO-1 crystal for phase matching, the SH spectra can be tuned from 505 to 555 nm with a high-power output. In detail, the SH center wavelength shifted by approximately 8.3 nm for every 5° variation in the phase-matching angle, and two higher powers of SH were achieved at 515 and 550 nm with an output power of 8.45 and 8.98 W, respectively, corresponding to the intensity peaks at 1030 and 1100 nm in the infrared spectrum. Three typical normalized SH spectra centered at 510, 532, and 545 nm are shown in Figure 3d, in which the uneven infrared spectral profile leads to different spectral half bandwidths of 16, 24, and 26 nm, respectively.

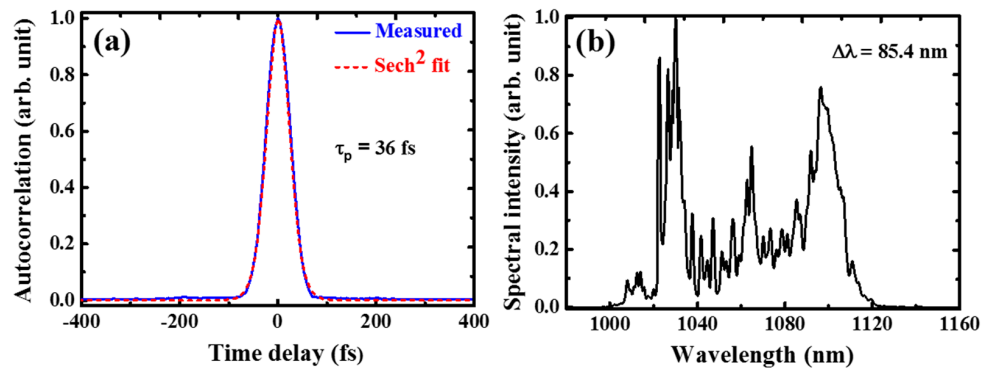


Figure 2. (a) Autocorrelation trace (blue line) of compressed infrared pulses with a fitting sech²-type curve (red dashes). (b) Corresponding output spectrum of the amplified infrared pulses. Both (a) and (b) were measured at an average power of 58.9 W.

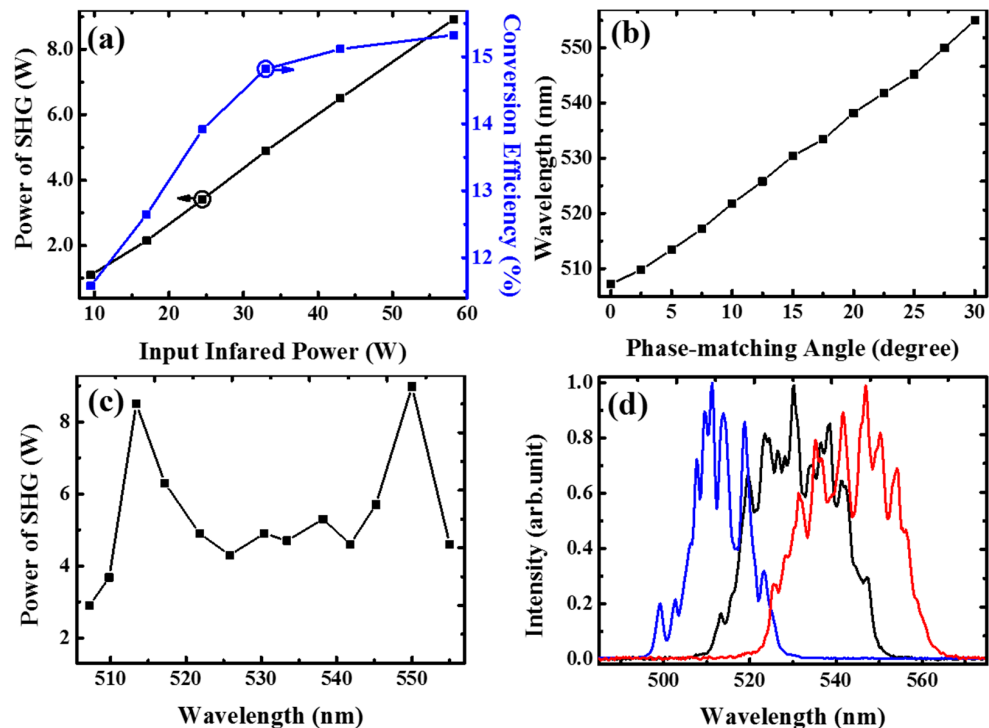


Figure 3. (a) Output power (black line) and conversion efficiency (blue line) of the SHG versus input infrared power. (b) Wavelength tuning property of the SHG. (c) Generated second harmonic (SH) power as a function of output wavelength. (d) Three typical normalized SH spectra.

Similarly to SHG, another 2 mm thick β -BBO crystal (BBO-2) with a cut angle of 49.4° was used to generate the fourth harmonic (FH). Through fine adjustment of the distance between L2 and L3, a suitable SH beam size on the L3 surface was chosen for the following frequency conversion in BBO-2. Subsequently, L3 focused the SH beam inside the center of BBO-2 with a calculated diameter of $30\ \mu\text{m}$. L4 was used to collimate the generated FH, and DM3 and DM4 were used to filter the unconverted SH. The data presented in Figure 4a were measured at 275 nm with BBO-1 operating at approximately 530 nm. The variations in the FH power and infrared-to-UV efficiency exhibited the same tendency as the SHG. A maximum FH power of 1.44 W was obtained at an infrared power of 58.9 W and the conversion efficiency of infrared-to-UV was 2.44%. The FH output wavelength as a function of the BBO-2 phase-matching angle is shown in Figure 4b, and the corresponding SH spectrum is also indicated by the red line in the inset of Figure 4b. The tunable spectral range of the output FH was 263–275 nm, and the center wavelength shifted by approximately 2 nm when the phase-matching angle of BBO-2 changed by 5° . In addition, a wider UV spectral range was obtained by simultaneously adjusting BBO-1 and BBO-2. Figure 4c,d show the recorded power features and spectral characteristics of the FHG. As shown in Figure 4c, the output spectra could be tuned in a broadband UV range from 253.6 to 275 nm, consistent with the tunable range of the SH. The output FH power as a function of the center wavelength corresponds to the power distributions of the infrared and SH pulses. Particularly, two clear UV power peaks of 1.42 and 1.44 W were separately observed at 256.7 and 275 nm, and the related power peaks were also discovered at 515 and 530 nm of the tunable SH spectrum, and 1027 and 1100 nm of the infrared spectrum, respectively. Nine typical normalized FH spectra with bandwidths varying from 1.1 to 1.3 nm are shown in Figure 4d, demonstrating the outstanding tunable property of the UV spectra.

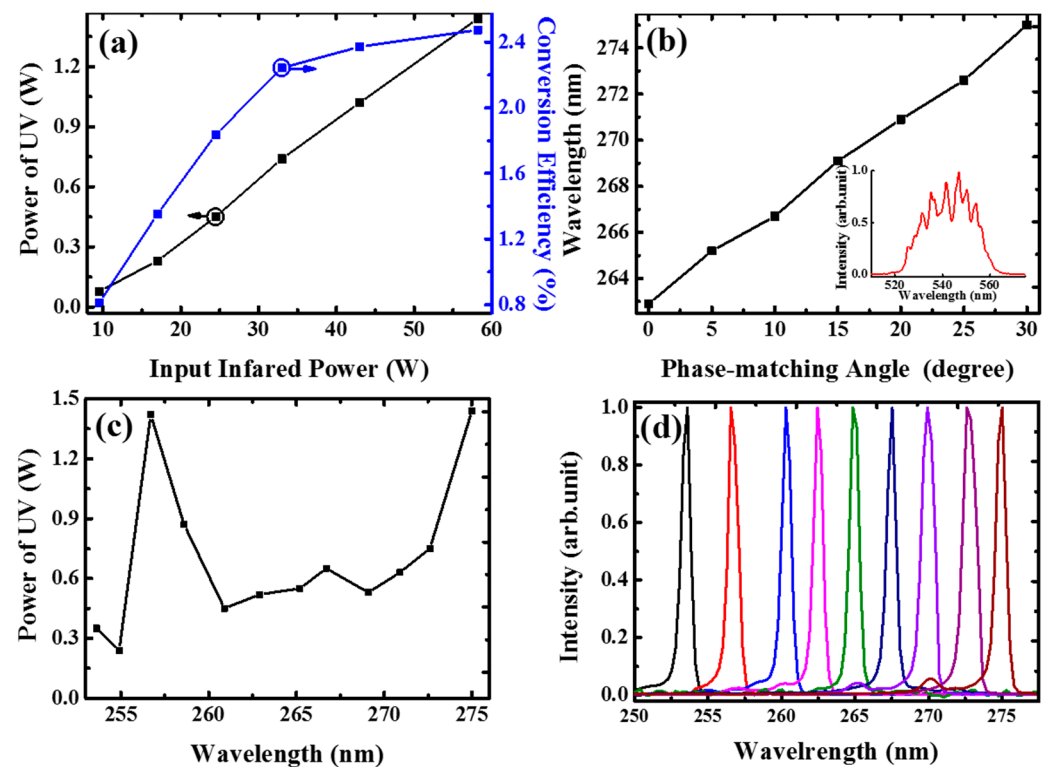


Figure 4. (a) Output power (black line) and infrared-to-ultraviolet conversion efficiency (blue line) of the FHG versus input infrared power. (b) Wavelength tunable property of the FHG (black line); the inset shows the second harmonic used for FHG (red line). (c) Generated fourth harmonic (FH) power as a function of output wavelength. (d) Nine typical normalized FH spectra.

4. Conclusions

In summary, a high-power tunable UV pulse generation through frequency quadrupling of high-power infrared pulses was demonstrated. A homemade NPR oscillator was employed as the seed laser and the output power was amplified to 8.4 W after the pre-amplifiers. Then, using a pre-chirping-management fiber SSA system, a 58.9 W, 36-fs infrared pulse train was obtained with a spectral half-width of 85.4 nm. Two cascaded β -BBO crystals were used to perform FHG in a simple single-pass configuration. Owing to the broadband infrared spectrum, the output visible spectra also had a broadband spectrum from 505 to 555 nm. Subsequently, the obtained UV spectra could be tuned in a broadband UV region, covering 253.6 to 275 nm. By adjusting the phase-matching angles of these crystals, the achieved maximum UV power reached up to 1.44 W at 275 nm, accompanied by a spectral half-width of 1.1 nm and an infrared-to-ultraviolet efficiency of 2.44%. To the best of our knowledge, this is the first study on the generation of broadband tunable UV pulses directly obtained from a fiber SSA. We believe that the tunable high-power UV pulses can be applied in many fields such as ultraviolet spectroscopy and precision metrology.

Author Contributions: Conceptualization, Z.W.; methodology, Z.W. and D.L.; software, Z.W. and Z.D.; validation, D.L., G.X. and Z.D.; formal analysis, Z.W. and G.X.; investigation, Z.W. and D.L.; resources, W.L.; data curation, Z.W. and D.L.; writing—original draft preparation, Z.W.; writing—review and editing, D.L. and C.G.; visualization, Z.W. and C.G.; supervision, D.L. and W.L.; project administration, W.L.; funding acquisition, W.L. All authors have read and agreed to the published version of the manuscript.

Funding: This research was funded by the National Natural Science Foundation of China (12134004, 62425503, 12274141, 12204178).

Institutional Review Board Statement: Not applicable.

Informed Consent Statement: Not applicable.

Data Availability Statement: Data are contained within the article.

Conflicts of Interest: The authors declare no conflicts of interest.

References

1. Ozaki, Y.; Kawata, S. (Eds.) *Far- and Deep-Ultraviolet Spectroscopy*; Springer: Tokyo, Japan, 2015.
2. Consani, C.; Auböck, G.; Van Mourik, F.; Chergui, M. Ultrafast Tryptophan-to-Heme Electron Transfer in Myoglobins Revealed by UV 2D Spectroscopy. *Science* **2013**, *339*, 1586–1589. [[CrossRef](#)] [[PubMed](#)]
3. Hassan, M.T.; Baskin, J.S.; Liao, B.; Zewail, A.H. High-temporal-resolution electron microscopy for imaging ultrafast electron dynamics. *Nat. Photon.* **2017**, *11*, 425–430. [[CrossRef](#)]
4. Cingöz, A.; Yost, D.C.; Allison, T.K.; Ruehl, A.; Fermann, M.E.; Hartl, I.; Ye, J. Direct frequency comb spectroscopy in the extreme ultraviolet. *Nature* **2012**, *482*, 68–71. [[CrossRef](#)] [[PubMed](#)]
5. Chipperfield, M.P.; Dhomse, S.S.; Feng, W.; McKenzie, R.L.; Velders, G.J.M.; Pyle, J.A. Quantifying the ozone and ultraviolet benefits already achieved by the Montreal Protocol. *Nat. Commun.* **2015**, *6*, 7233. [[CrossRef](#)]
6. Khan, S.; Newport, D.; Le Calvé, S. Gas Detection Using Portable Deep-UV Absorption Spectrophotometry: A Review. *Sensors* **2019**, *19*, 5210. [[CrossRef](#)]
7. Zhang, Y.G.; Wang, H.S.; Somesfalean, G.; Wang, Z.Y.; Lou, X.T.; Wu, S.H.; Zhang, Z.G.; Qin, Y.K. Broadband UV spectroscopy system used for monitoring of SO₂ and NO emissions from thermal power plants. *Atmos. Environ.* **2010**, *44*, 4266–4271. [[CrossRef](#)]
8. Hachisu, H.; Miyagishi, K.; Porsev, S.G.; Derevianko, A.; Ovsiannikov, V.D.; Pal'chikov, V.G.; Takamoto, M.; Katori, H. Trapping of Neutral Mercury Atoms and Prospects for Optical Lattice Clocks. *Phys. Rev. Lett.* **2008**, *100*, 053001. [[CrossRef](#)]
9. Kaneda, Y.; Yarborough, J.M.; Merzlyak, Y.; Yamaguchi, A.; Hayashida, K.; Ohmae, N.; Katori, H. Continuous-wave, single-frequency 229 nm laser source for laser cooling of cadmium atoms. *Opt. Lett.* **2016**, *41*, 705–708. [[CrossRef](#)]
10. Xu, H.; Lu, H.; Li, Z.; Zhao, J. Deep-ultraviolet femtosecond laser source at 243 nm for hydrogen spectroscopy. *Opt. Express* **2021**, *29*, 17398–17404. [[CrossRef](#)]
11. Altmann, R.K.; Galtier, S.; Dreissen, L.S.; Eikema, K.S.E. High-Precision Ramsey-Comb Spectroscopy at Deep Ultraviolet Wavelengths. *Phys. Rev. Lett.* **2016**, *117*, 173201. [[CrossRef](#)]

12. Thyagarajan, K.; Santschi, C.; Langlet, P.; Martin, O.J.F. Highly Improved Fabrication of Ag and Al Nanostructures for UV and Nonlinear Plasmonics. *Adv. Opt. Mater.* **2016**, *4*, 871–876. [[CrossRef](#)]
13. Marques, C.A.F.; Antunes, P.; Mergo, P.; Webb, D.J.; André, P. Chirped Bragg Gratings in PMMA Step-Index Polymer Optical Fiber. *IEEE Photonics Technol. Lett.* **2017**, *29*, 500–503. [[CrossRef](#)]
14. Larciprete, R.; Stuke, M. Direct observation of excimer-laser photoablation products from polymers by picosecond-uv-laser mass spectroscopy. *Appl. Phys. B* **1987**, *42*, 181–184. [[CrossRef](#)]
15. Barmina, E.V.; Barberoglu, M.; Zorba, V.; Simakin, A.V. Surface nanotexturing of tantalum by laser ablation in water. *Quantum Electron.* **2009**, *39*, 89. [[CrossRef](#)]
16. Nabekawa, Y.; Yoshitomi, D.; Sekikawa, T.; Watanabe, S. High-average-power femtosecond KrF excimer laser. *IEEE J. Sel. Top. Quantum Electron.* **2001**, *7*, 551–558. [[CrossRef](#)]
17. Tzankov, P.; Fiebig, T.; Buchvarov, I. Tunable femtosecond pulses in the near-ultraviolet from ultrabroadband parametric amplification. *Appl. Phys. Lett.* **2003**, *82*, 517–519. [[CrossRef](#)]
18. Ghotbi, M.; Esteban-Martin, A.; Ebrahim-Zadeh, M. Tunable, high-repetition-rate, femtosecond pulse generation in the ultraviolet. *Opt. Lett.* **2008**, *33*, 345–347. [[CrossRef](#)]
19. Gu, C.; Hu, M.; Fan, J.; Song, Y.; Liu, B.; Chai, L.; Wang, C.; Reid, D.T. High power tunable femtosecond ultraviolet laser source based on an Yb-fiber-laser pumped optical parametric oscillator. *Opt. Express* **2015**, *23*, 6181–6186. [[CrossRef](#)]
20. Chaitanya, N.A.; Aadhi, A.; Jabir, M.V.; Samanta, G.K. High-power, high-repetition-rate, Yb-fiber laser based femtosecond source at 355 nm. *Opt. Lett.* **2015**, *40*, 4269–4272. [[CrossRef](#)]
21. Zhai, S.Y.; Wang, X.L.; Wei, Y.; Chen, W.D.; Zhuang, F.J.; Xu, S.; Li, B.X.; Fu, J.J.; Chen, Z.Q.; Wang, H.W.; et al. A compact efficient deep ultraviolet laser at 266 nm. *Laser Phys. Lett.* **2013**, *10*, 045402. [[CrossRef](#)]
22. Wang, G.; Geng, A.; Bo, Y.; Li, H.; Sun, Z.; Bi, Y.; Cui, D.; Xu, Z.; Yuan, X.; Wang, X.; et al. 28.4W 266nm ultraviolet-beam generation by fourth-harmonic generation of an all-solid-state laser. *Opt. Commun.* **2006**, *259*, 820–822. [[CrossRef](#)]
23. Willenberg, B.; Brunner, F.; Phillips, C.R.; Keller, U. High-power picosecond deep-UV source via group velocity matched frequency conversion. *Optica* **2020**, *7*, 485–491. [[CrossRef](#)]
24. Reiter, F.; Graf, U.; Schultze, M.; Schweinberger, W.; Schröder, H.; Karpowicz, N.; Azzeer, A.M.; Kienberger, R.; Krausz, F.; Goulielmakis, E. Generation of sub-3 fs pulses in the deep ultraviolet. *Opt. Lett.* **2010**, *35*, 2248–2250. [[CrossRef](#)] [[PubMed](#)]
25. Kosma, K.; Trushin, S.A.; Schmid, W.E.; Fuß, W. Vacuum ultraviolet pulses of 11 fs from fifth-harmonic generation of a Ti:sapphire laser. *Opt. Lett.* **2008**, *33*, 723–725. [[CrossRef](#)]
26. Kida, Y.; Liu, J.; Teramoto, T.; Kobayashi, T. Sub-10 fs deep-ultraviolet pulses generated by chirped-pulse four-wave mixing. *Opt. Lett.* **2010**, *35*, 1807–1809. [[CrossRef](#)]
27. Chen, C.; Wu, Y.; Jiang, A.; Wu, B.; You, G.; Li, R.; Lin, S. New nonlinear-optical crystal: LiB₃O₅. *J. Opt. Soc. Am. B* **1989**, *6*, 616–621. [[CrossRef](#)]
28. Nikogosyan, D.N. Beta barium borate (BBO): A review of its properties and applications. *Appl. Phys. A* **1991**, *52*, 359–368. [[CrossRef](#)]
29. Kienle, F.; Teh, P.S.; Lin, D.; Alam, S.; Price, J.H.V.; Hanna, D.C.; Richardson, D.J.; Shepherd, D.P. High-power, high repetition-rate, green-pumped, picosecond LBO optical parametric oscillator. *Opt. Express* **2012**, *20*, 7008–7014. [[CrossRef](#)]
30. Poberaj, G.; Degl’Innocenti, R.; Medrano, C.; Günter, P. UV integrated optics devices based on beta-barium borate. *Opt. Mater.* **2009**, *31*, 1049–1053. [[CrossRef](#)]
31. Köttig, F.; Tani, F.; Biersach, C.M.; Travers, J.C.; Russell, P.S.J. Generation of microjoule pulses in the deep ultraviolet at megahertz repetition rates. *Optica* **2017**, *4*, 1272–1276. [[CrossRef](#)]
32. Zhou, X.; Yoshitomi, D.; Kobayashi, Y.; Torizuka, K. 1 W average-power 100 MHz repetition-rate 259 nm femtosecond deep ultraviolet pulse generation from ytterbium fiber amplifier. *Opt. Lett.* **2010**, *35*, 1713–1715. [[CrossRef](#)] [[PubMed](#)]
33. Yang, K.; Li, W.; Yan, M.; Shen, X.; Zhao, J.; Zeng, H. High-power ultra-broadband frequency comb from ultraviolet to infrared by high-power fiber amplifiers. *Opt. Express* **2012**, *20*, 12899–12905. [[CrossRef](#)] [[PubMed](#)]
34. Fermann, M.E.; Kruglov, V.I.; Thomsen, B.C.; Dudley, J.M.; Harvey, J.D. Self-Similar Propagation and Amplification of Parabolic Pulses in Optical Fibers. *Phys. Rev. Lett.* **2000**, *84*, 6010–6013. [[CrossRef](#)] [[PubMed](#)]
35. Zhao, J.; Li, W.; Wang, C.; Liu, Y.; Zeng, H. Pre-chirping management of a self-similar Yb-fiber amplifier towards 80 W average power with sub-40 fs pulse generation. *Opt. Express* **2014**, *22*, 32214–32219. [[CrossRef](#)]
36. Liu, Y.; Li, W.; Luo, D.; Bai, D.; Wang, C.; Zeng, H. Generation of 33 fs 935 W average power pulses from a third-order dispersion managed self-similar fiber amplifier. *Opt. Express* **2016**, *24*, 10939–10945. [[CrossRef](#)]
37. Luo, D.; Liu, Y.; Gu, C.; Wang, C.; Zhu, Z.; Zhang, W.; Deng, Z.; Zhou, L.; Li, W.; Zeng, H. High-power Yb-fiber comb based on pre-chirped-management self-similar amplification. *Appl. Phys. Lett.* **2018**, *112*, 061106. [[CrossRef](#)]
38. Tamura, K.; Ippen, E.P.; Haus, H.A.; Nelson, L.E. 77-fs pulse generation from a stretched-pulse mode-locked all-fiber ring laser. *Opt. Lett.* **1993**, *18*, 1080–1082. [[CrossRef](#)]

39. Yang, S.; Zhu, Z.; He, C.; Shi, Y.; Yang, Y.; Lin, X. Collapse of pure-quartic solitons in a mode-locked fiber laser. *Chaos Solitons Fractals* **2024**, *180*, 114538. [[CrossRef](#)]
40. Yang, S.; Zhu, Z.; Qi, Y.; Jin, L.; Li, L.; Lin, X. Internal motion within pulsating pure-quartic soliton molecules in a fiber laser. *Chaos Solitons Fractals* **2023**, *172*, 113544. [[CrossRef](#)]
41. Luo, D.; Li, W.; Liu, Y.; Wang, C.; Zhu, Z.; Zhang, W.; Zeng, H. High-power self-similar amplification seeded by a 1 GHz harmonically mode-locked Yb-fiber laser. *Appl. Phys. Express* **2016**, *9*, 082702. [[CrossRef](#)]
42. Shah, L.; Fermann, M. High-Power Ultrashort-Pulse Fiber Amplifiers. *IEEE J. Sel. Top. Quantum Electron.* **2007**, *13*, 552–558. [[CrossRef](#)]
43. Armstrong, J.A.; Bloembergen, N.; Ducuing, J.; Pershan, P.S. Interactions between Light Waves in a Nonlinear Dielectric. *Phys. Rev.* **1962**, *127*, 1918–1939. [[CrossRef](#)]
44. Baumgartner, R.; Byer, R. Optical parametric amplification. *IEEE J. Quantum Electron.* **1979**, *15*, 432–444. [[CrossRef](#)]

Disclaimer/Publisher’s Note: The statements, opinions and data contained in all publications are solely those of the individual author(s) and contributor(s) and not of MDPI and/or the editor(s). MDPI and/or the editor(s) disclaim responsibility for any injury to people or property resulting from any ideas, methods, instructions or products referred to in the content.